Supporting information for

# Unveiling the distinct structure of the upper mantle beneath the Canary and Madeira hotspots, as depicted by the 660, 410 and X discontinuities

Luciana Bonatto[a], David Schlaphorst[b], Graça Silveira[b,c], João Mata[b], Chiara Civiero[d,e], Claudia Piromallo[f], and Martin Schimmel[g]

[a]Departamento de Física de la Universidad de La Serena, Av. Juan Cisternas, 1200, La Serena, 1700000, Coquimbo, Chile

[b]Faculdade de Ciências, Instituto Dom Luiz (IDL), Universidade de Lisboa, Campo Grande, 1749-016, Lisbon, Portugal

[c]Instituto Superior de Engenharia de Lisboa, Rua Conselheiro Emídio Navarro 1, Lisbon, 1959-007, Portugal

[d]Institut de Ciències del Mar, ICM-CSIC, Pg. Marítim de la Barceloneta, 37, Barcelona, 08003, Spain

[e]Dipartimento di Matematica e Geoscienze, Università di Trieste, via Weiss 2, Trieste, 34128, Italy.

[f]Istituto Nazionale di Geofisica e Vulcanologia, Via di Vigna Murata, 605, Rome, 00143, Italy

[g]GeoSciences Barcelona, Geo3Bcn, CSIC, c/ Solé Sabarís sn, Barcelona, 08028, Spain

## Contents of this file

**Section 3 and Figures S12 to S15**: Robustness analysis to assess the accuracy of time-to-depth conversions

**Table S3**: Possible mechanisms for the X discontinuity.

# 1 Processing to compute receiver functions

We compute RFs using the processing methods outlined in Bonatto et al. (2015, 2020). Here, we provide a comprehensive review of the process. We apply an initial quality control to keep the traces with strong signal in the vertical component, i.e. first arrival with large amplitude. To do this, we implement an energy-based event detection technique known as the STA/LTA algorithm (Allen, 1978) which is based on observing the changes in the amplitudes of a single seismic trace within moving time windows. We apply a low-pass filter of 0.12 Hz to the Z component and use STA and LTA values of 10 s and 100 s, respectively. We keep the waveforms with an STA/LTA ratio larger than 2.7.

To compute the RFs, we rotate the $Z, N, E$ components into the $(Z, R, T)$ system and cut them around the first arrival (120 s before to 220 s after). Then, we apply standard pre-processing steps to the waveforms. First, we remove the mean and the trend. Then, we band-pass filtered the three rotated components between 0.02 Hz and 0.12 Hz. Ultimately, we downsample the traces to 20 samples per second and define a pilot trace ($P_Z$) from the Z component for deconvolution. The Z waveform is windowed from 25 before to 75 s after the onset of the $P$-phase and a cosine taper of 5 seconds is used to avoid signal processing artifacts in the remaining processing.

We perform the deconvolution of the $P_Z$ from the $R$ component in the spectral domain, which implies a spectral division ($P_R(\omega)\bar{P}_R(\omega)/P_Z(\omega)\bar{P}_Z(\omega)$). To stabilize the spectral division, we use the water-level deconvolution (Clayton and Wiggins, 1976) with a water-level parameter of 0.01. Then, deconvolved traces are shifted to center the P-phase pulse at zero time. Finally, the RF is the deconvolved radial component.

Three quality controls are applied on individual RFs: an automatic quality control and two visual quality controls. The automatic quality control is based on the signal-to-noise ratio (SNR). For this, we calculate the *rms* of the background signal 35 and 5 s before the $P$-phase (*noise*), and the rms of the main signal 5 s before and 25 s after the $P$-phase (*signal*). We keep the RFs

that meet the following criteria: $SNR > 1.4$. The first visual quality control is performed over the three deconvolved components (Z, R, and T). We visually inspect the deconvolved components and check that they meet the following criteria:

1. Low noise level before the first arrival in the RF (deconvolver $R$ waveform); unstable deconvolution often results in large amplitude prior to the initial $P$-wave peak.

2. A clear peak at $t = 0$ s in the deconvolved $Z$ component with small side-lobes. For larger times, the trace should have small amplitudes. This is because all converted phases and multiples are expected with amplitudes smaller than 10 per cent of the $P$-phase amplitude. Therefore, large amplitude signals at $t > 0$ s correspond to other main phases such as $PP$, $PcP$, etc., which for certain distances have similar arrival times to that of the converted phases at upper-mantle discontinuities between 200 km and 700 km.

3. Very small amplitudes in the deconvolved $T$ component. This is because for teleseismic earthquakes (i.e., vertical incidence angles), this component only records $SH$ phases and converted $SH$ energy is only expected in cases of strong discontinuity topography or strong anisotropy above the discontinuities.

Lastly, we visually inspect the RFs plotted versus their back-azimuths at each seismic station and we discard traces with low-quality results. This final step ensures that we only keep traces that are similar.

Ultimately, using raw ZNT triplets associated with RFs that have passed all quality controls in the lower frequency band, we compute new RFs with a lower cut-off frequency at $f_1 = 0.02$ Hz and higher cut-off frequencies at $f_2 = 0.20$, 0.32, 0.48, and 0.64 Hz.

Table S1: Geographical coordinates of the stations, number of teleseismic records per stations and number of good quality receiver functions.

| Network.Station | latitude [°] | longitude [°] | N° of Records | N° of RFs |
|---|---|---|---|---|
| *Stations in the Canary Islands* | | | | |
| ES.CBOL | 28.3144 | -16.8306 | 64 | 0 |
| ES.CCAL | 27.7128 | -18.1472 | 59 | 3 |
| ES.CCAN | 28.2217 | -16.6050 | 330 | 6 |
| ES.CCUM | 27.7459 | -18.0301 | 636 | 6 |
| ES.CFUE | 28.6468 | -13.9359 | 1142 | 224 |
| ES.CGIN | 28.2054 | -14.0823 | 307 | 8 |
| ES.CGUI | 28.3222 | -16.4425 | 456 | 4 |
| ES.CJUL | 27.7296 | -18.0823 | 67 | 0 |
| ES.CLOB | 28.7649 | -13.8149 | 293 | 16 |
| ES.CNAO | 27.6470 | -17.9883 | 87 | 0 |
| ES.CNOR | 28.3135 | -16.6600 | 73 | 0 |
| ES.CRAJ | 28.2649 | -16.5969 | 1203 | 57 |
| ES.CTAB | 27.7494 | -18.0850 | 653 | 32 |
| ES.CTAN | 27.7544 | -18.0543 | 688 | 17 |
| ES.CTIG | 27.7882 | -17.9221 | 882 | 68 |
| ES.CVIL | 28.1593 | -16.6425 | 72 | 0 |
| ES.EBAJ | 28.5399 | -16.3434 | 1131 | 18 |
| ES.EFAM | 29.1275 | -13.5295 | 1214 | 110 |
| ES.EGOM | 28.1594 | -17.2096 | 1135 | 105 |
| ES.EHIG | 28.5567 | -17.8062 | 1217 | 130 |
| ES.EOSO | 28.0718 | -15.5525 | 801 | 78 |
| ES.GGC | 28.1197 | -15.6367 | 319 | 11 |
| IU.MACI | 28.2502 | -16.5082 | 480 | 56 |
| ES.TBT | 28.6794 | -17.9145 | 269 | 0 |
| | | *Total* | *13578* | *948* |
| *Stations in Madeira* | | | | |
| Y7.DOC-01 | 32.7184 | -16.9729 | 203 | 13 |
| Y7.DOC-02 | 32.7651 | -16.9235 | 171 | 8 |
| Y7.DOC-05 | 32.6838 | -16.9495 | 198 | 19 |
| Y7.DOC-06 | 32.8090 | -16.9099 | 202 | 7 |
| Y7.DOC-07 | 32.7896 | -17.1095 | 200 | 11 |
| Y7.DOC-08 | 32.6984 | -17.0832 | 199 | 13 |
| Y7.DOC-09 | 32.7371 | -17.1538 | 203 | 13 |
| Y7.DOC-10 | 32.8248 | -16.9900 | 203 | 12 |
| Y7.DOC-11 | 32.7484 | -16.7954 | 202 | 7 |
| Y7.DOC-12 | 32.5145 | -16.5094 | 198 | 9 |
| Y7.DOC-13 | 32.7459 | -16.9626 | 198 | 9 |
| Y7.DOC-16 | 32.7536 | -17.0156 | 202 | 14 |
| Y7.DOC-21 | 32.7234 | -16.8292 | 200 | 7 |
| Y7.DOC-22 | 32.8092 | -17.1405 | 202 | 8 |
| Y7.DOC-23 | 32.7973 | -16.9714 | 197 | 7 |
| Y7.DOC-24 | 32.7943 | -16.8819 | 201 | 8 |
| PM.PMOZ | 32.8230 | -17.1972 | 1772 | 80 |
| PM.PMPST | 33.0788 | -16.3333 | 1524 | 75 |
| | | *Total* | *6475* | *320* |

ES: Spanish Digital Seismic Network ; IU: Global Seismograph Network; Y7: Deep OCean Test ARray experiment (DOCTAR); PM: Portuguese National Seismic Network

# 2 Quality control of vespagrams for P300s

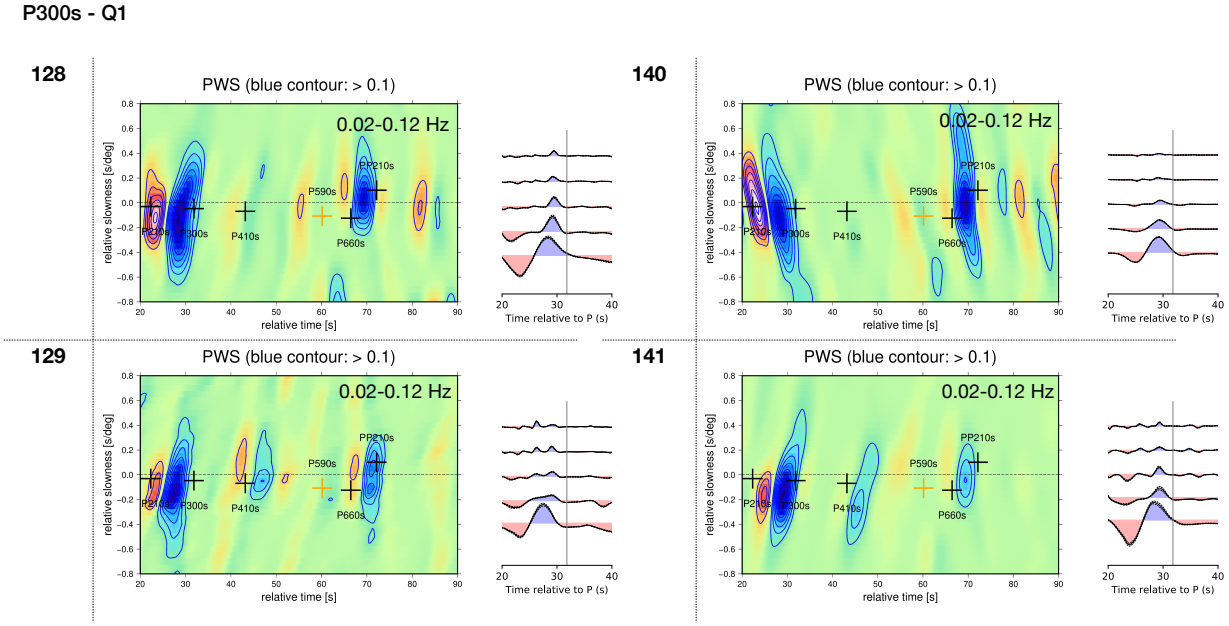


Figure S1: Examples of quality 1 stacks for P300s. Stacks with fixed estimated slowness at different frequency bands (0.02-0.12 Hz, 0.02-0.2 Hz, 0.02-0.32 Hz, 0.02-0.48 Hz, 0.02-0.64 Hz) are only shown for all CCP stacks. Discarded stacks and the reasons for their exclusion are highlighted in red.

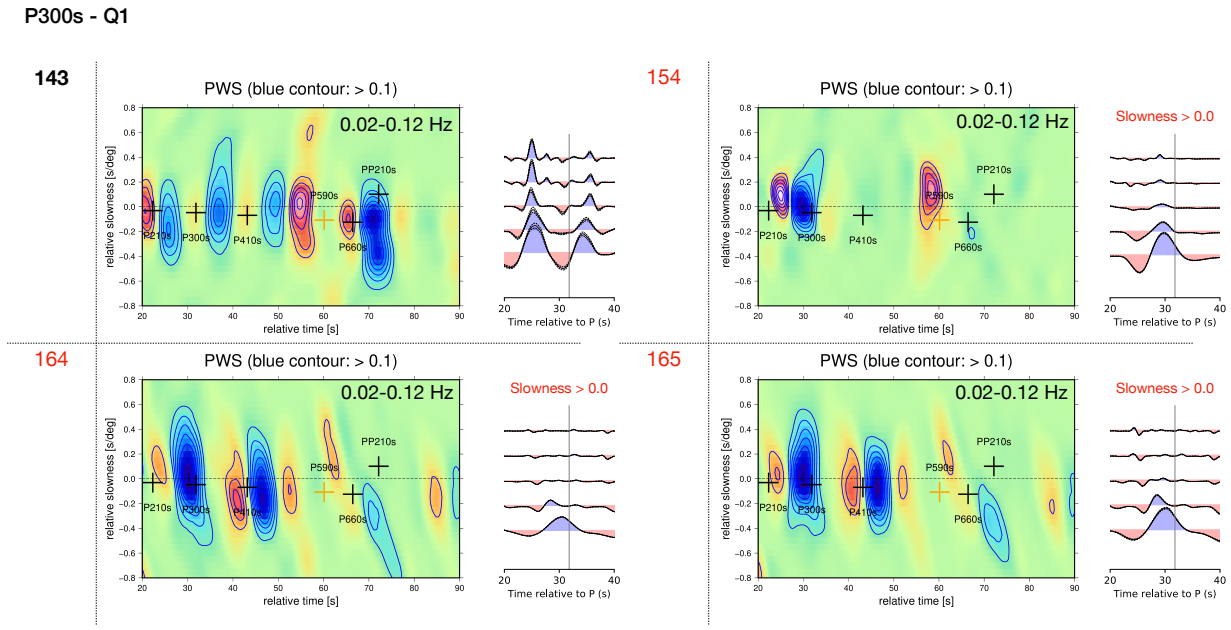


Figure S2: Examples of quality 1 stacks for P300s. Stacks with fixed estimated slowness at different frequency bands (0.02-0.12 Hz, 0.02-0.2 Hz, 0.02-0.32 Hz, 0.02-0.48 Hz, 0.02-0.64 Hz) are only shown for all CCP stacks. Discarded stacks and the reasons for their exclusion are highlighted in red.

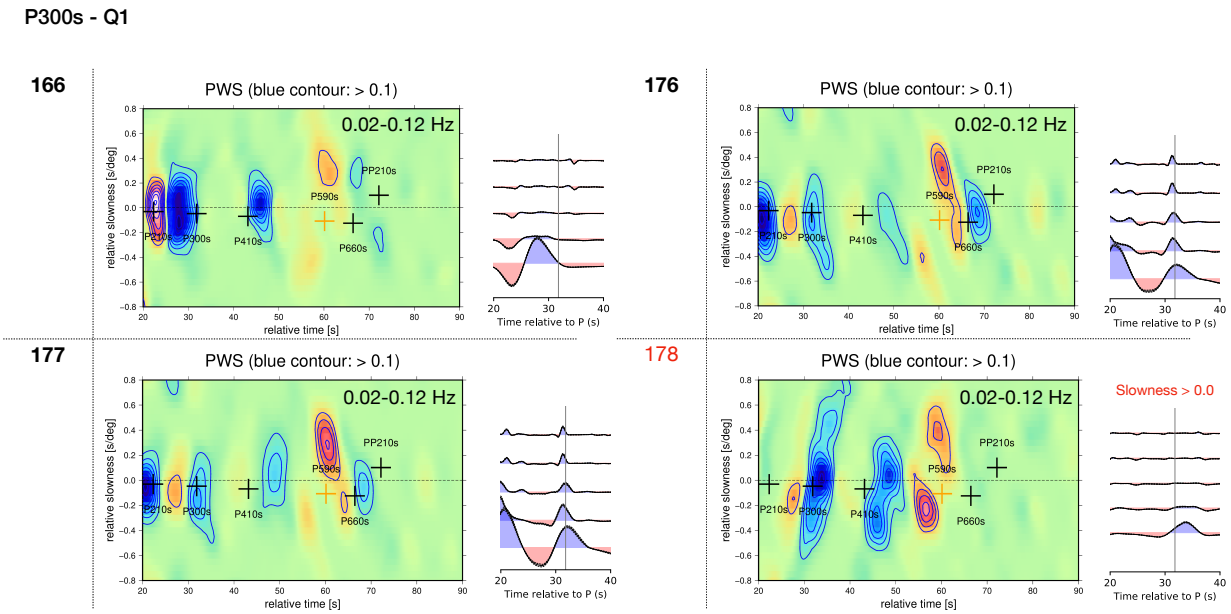


Figure S3: Examples of quality 1 stacks for P300s. Stacks with fixed estimated slowness at different frequency bands (0.02-0.12 Hz, 0.02-0.2 Hz, 0.02-0.32 Hz, 0.02-0.48 Hz, 0.02-0.64 Hz) are only shown for all CCP stacks. Discarded stacks and the reasons for their exclusion are highlighted in red.

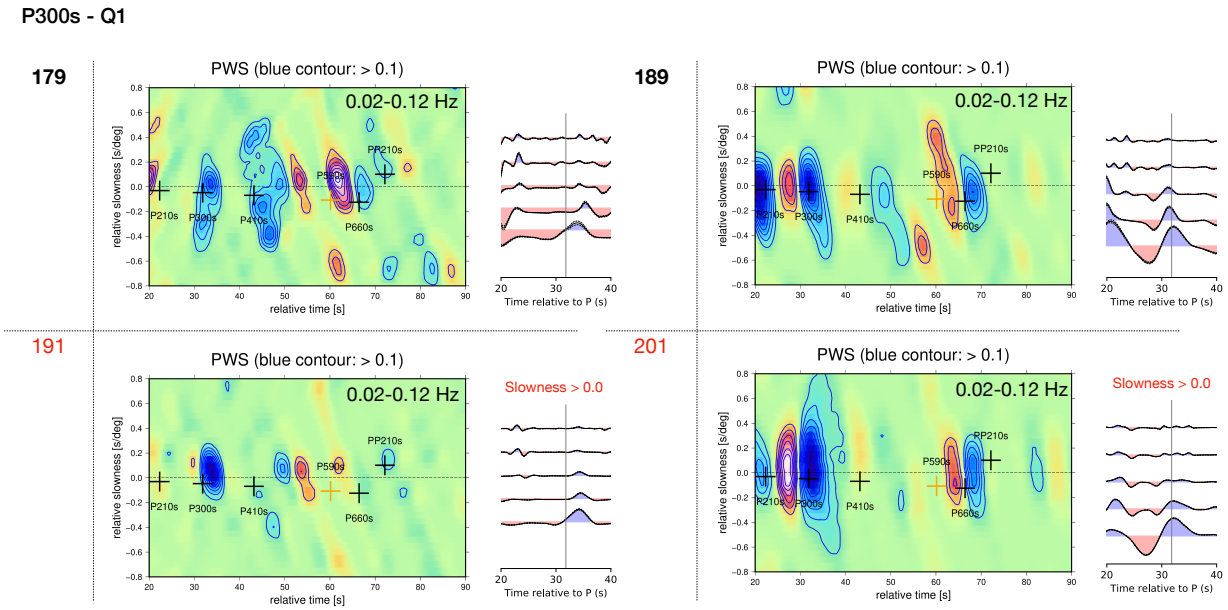


Figure S4: Examples of quality 2 stacks in the Canaries for P300s. Stacks with fixed estimated slowness at different frequency bands (0.02-0.12 Hz, 0.02-0.2 Hz, 0.02-0.32 Hz, 0.02-0.48 Hz, 0.02-0.64 Hz) are only shown for all CCP stacks. Discarded stacks and the reasons for their exclusion are highlighted in red.

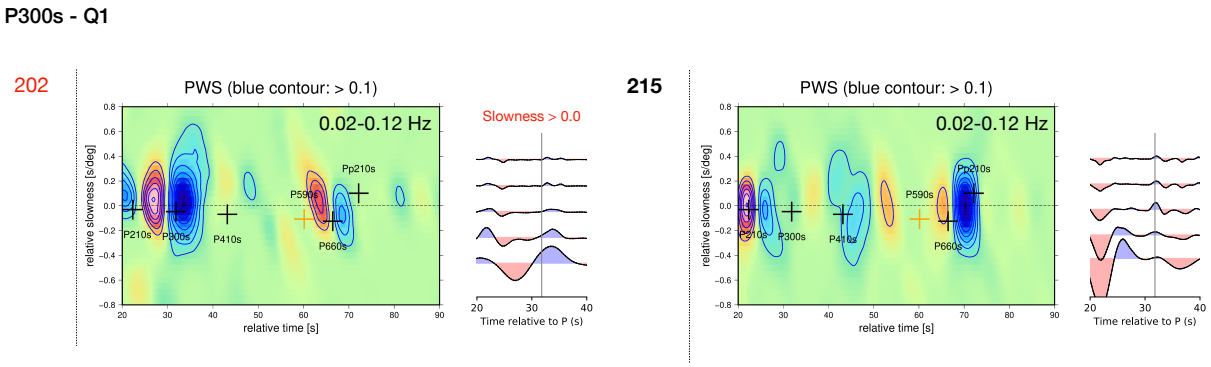


Figure S5: Examples of quality 1 stacks in the Canaries for P300s. Stacks with fixed estimated slowness at different frequency bands (0.02-0.12 Hz, 0.02-0.2 Hz, 0.02-0.32 Hz, 0.02-0.48 Hz, 0.02-0.64 Hz) are only shown for all CCP stacks. Discarded stacks and the reasons for their exclusion are highlighted in red.

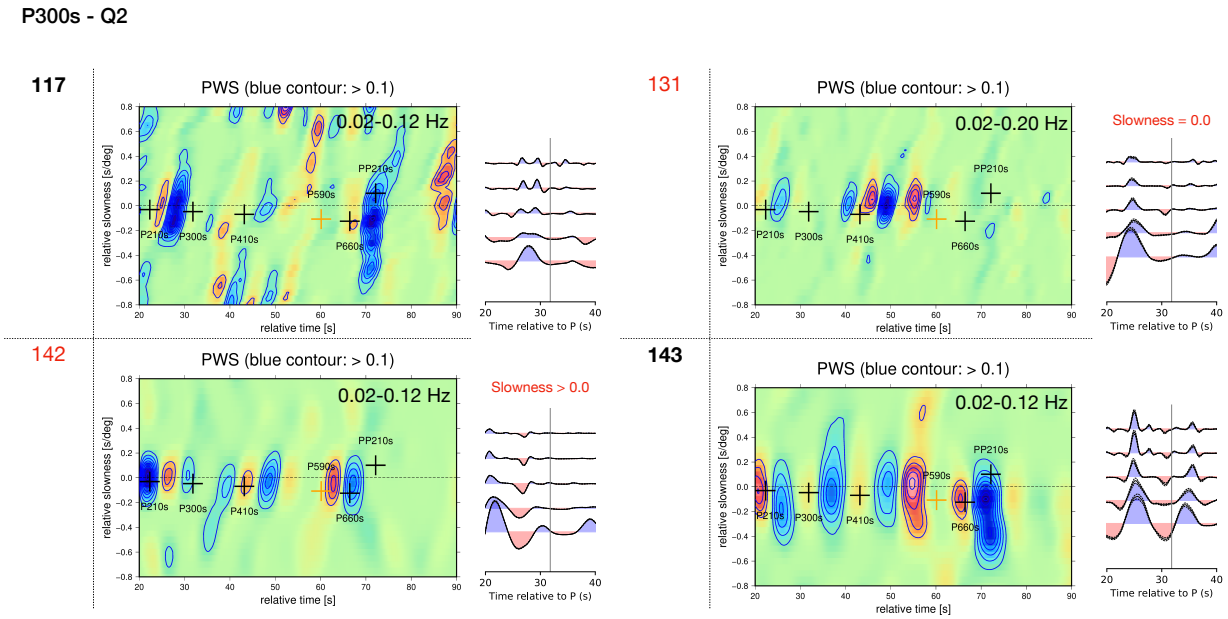


Figure S6: Examples of quality 2 stacks in the Canaries for P300s. Stacks with fixed estimated slowness at different frequency bands (0.02-0.12 Hz, 0.02-0.2 Hz, 0.02-0.32 Hz, 0.02-0.48 Hz, 0.02-0.64 Hz) are only shown for all CCP stacks. Discarded stacks and the reasons for their exclusion are highlighted in red.

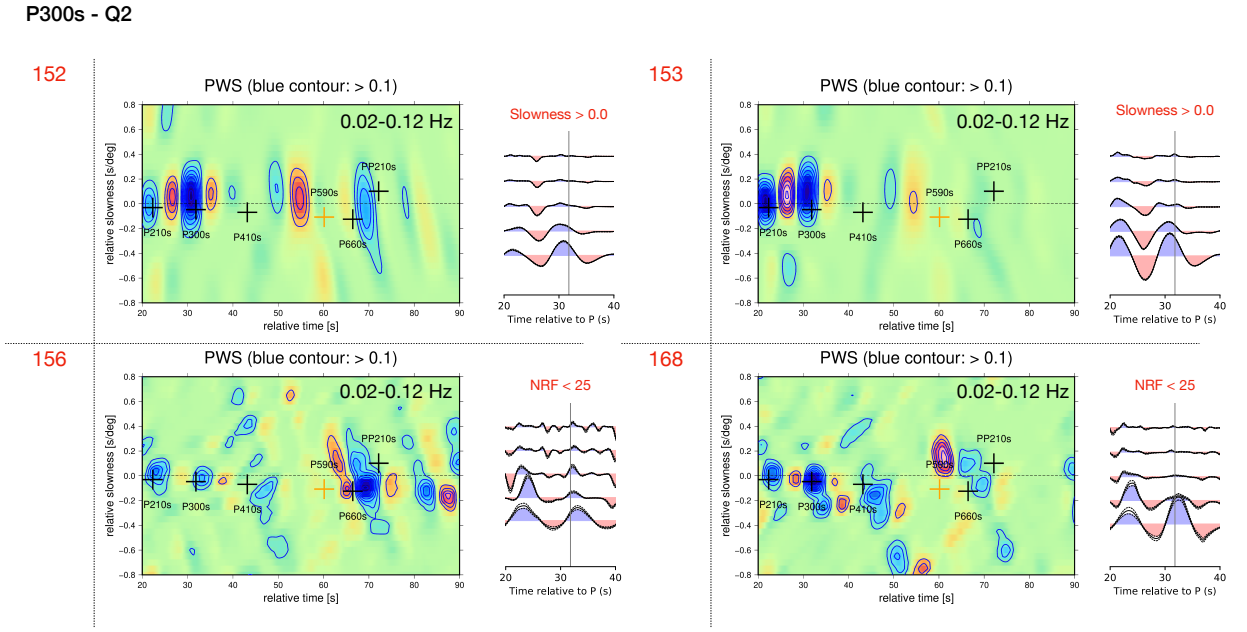


Figure S7: Examples of quality 2 stacks in the Canaries for P300s. Stacks with fixed estimated slowness at different frequency bands (0.02-0.12 Hz, 0.02-0.2 Hz, 0.02-0.32 Hz, 0.02-0.48 Hz, 0.02-0.64 Hz) are only shown for all CCP stacks. Discarded stacks and the reasons for their exclusion are highlighted in red.

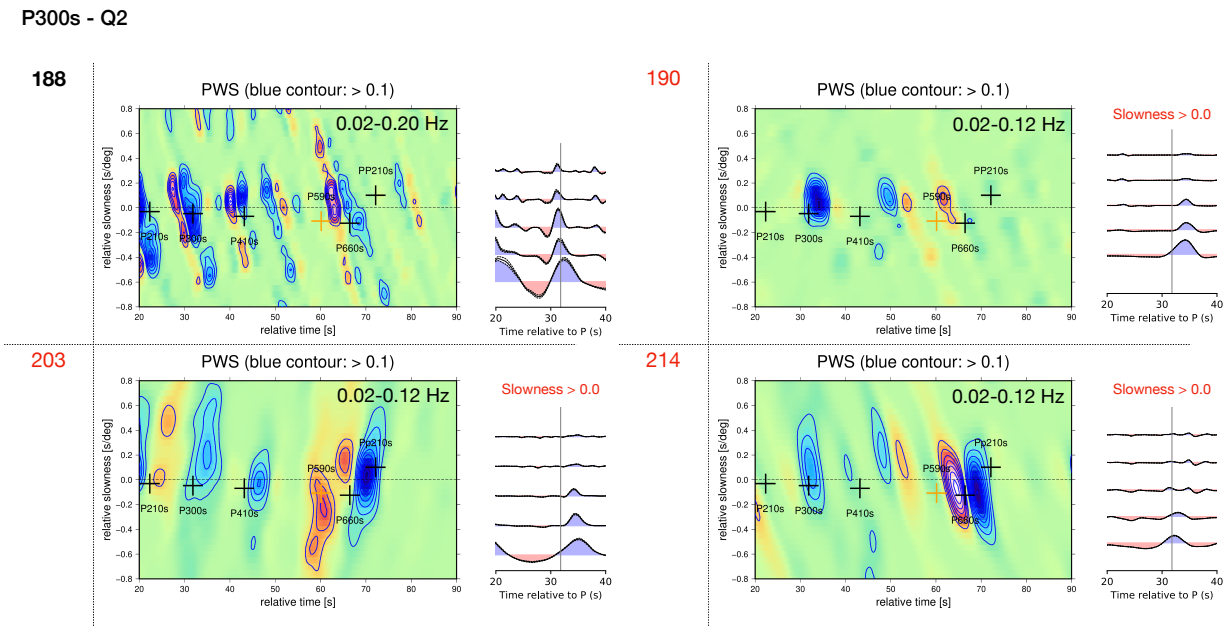


Figure S8: Examples of quality 2 stacks in the Canaries for P300s. Stacks with fixed estimated slowness at different frequency bands (0.02-0.12 Hz, 0.02-0.2 Hz, 0.02-0.32 Hz, 0.02-0.48 Hz, 0.02-0.64 Hz) are only shown for all CCP stacks. Discarded stacks and the reasons for their exclusion are highlighted in red.

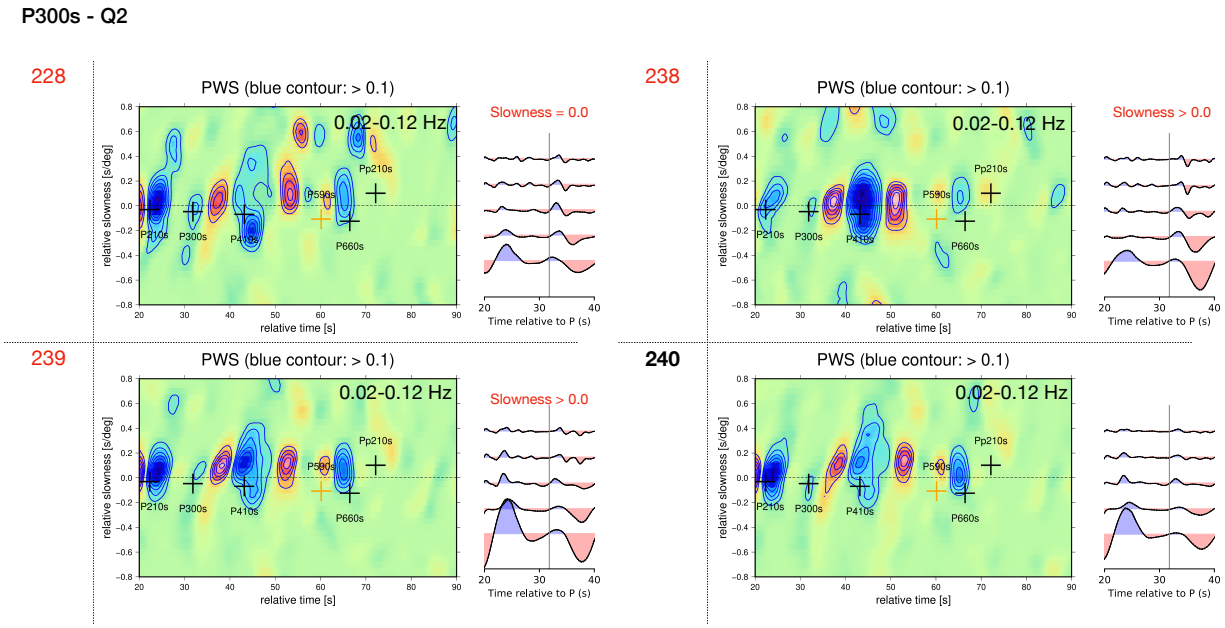


Figure S9: Examples of quality 2 stacks in the Canaries for P300s. Stacks with fixed estimated slowness at different frequency bands (0.02-0.12 Hz, 0.02-0.2 Hz, 0.02-0.32 Hz, 0.02-0.48 Hz, 0.02-0.64 Hz) are only shown for all CCP stacks. Discarded stacks and the reasons for their exclusion are highlighted in red.

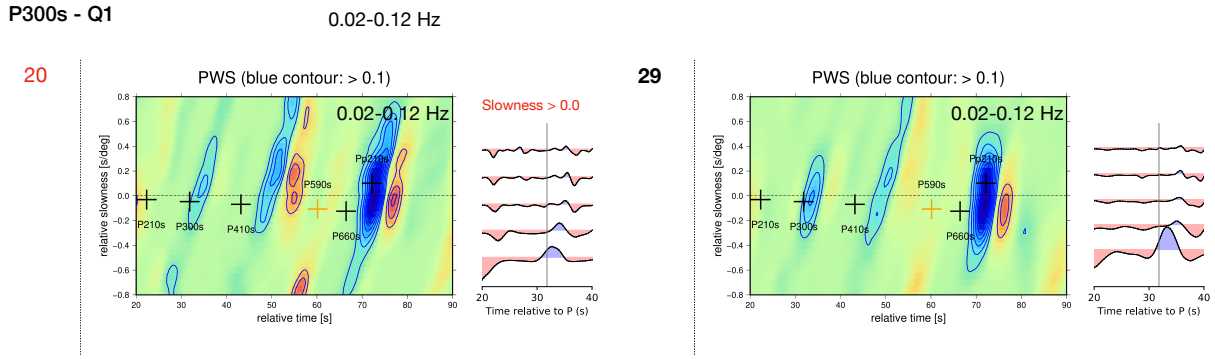


Figure S10: Examples of quality 1 stacks in Madeira for P300s. Stacks with fixed estimated slowness at different frequency bands (0.02-0.12 Hz, 0.02-0.2 Hz, 0.02-0.32 Hz, 0.02-0.48 Hz, 0.02-0.64 Hz) are only shown for all CCP stacks. Discarded stacks and the reasons for their exclusion are highlighted in red.

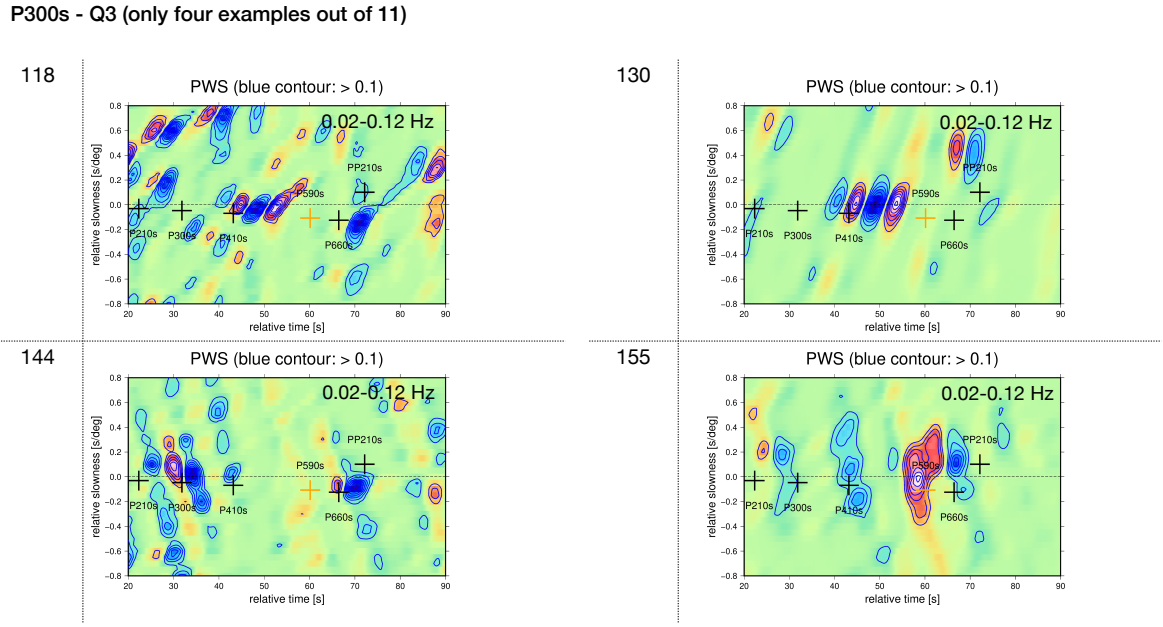


Figure S11: Examples of quality 3 stacks for P300s.

# 3 Robustness analysis

The absolute depth of discontinuities is determined by the velocity model used to correct the observed times. Underestimation of anomalies in tomography models is a significant concern when making corrections as it can lead to underestimation of time corrections. To overcome this issue, we doubled the value of the velocity anomalies in both tomography models, IBEM-P18/-S19 and MIT-P08. Incorrect determination of time corrections could lead to an inaccurate estimation of the depth of discontinuities. Therefore, when assessing the accuracy of time-to-depth conversions, it is a common procedure to examine the correlation between the topography of the 410 and 660 discontinuities (e.g. Bonatto et al., 2020; Boyce and Cottaar, 2021; Dueker and Sheehan, 1998). To do so, the topography of the 410 and 660 is assumed to be influenced by the temperature of the MTZ. In hot/cold MTZ where olivine is the dominant mineral, the correlation of the topography is expected to be negative due to the opposite sign of the Clapeyron slopes for the 410 and 660. These scenarios are illustrated in quadrants II and IV of Fig. S12. Conversely, positive correlation values between the depths of the 410 and 660 are indicative of underestimates or overestimates of the time corrections. However, if the dominant mineral in the TZ is garnet, the Clapeyron slopes of the 410 and 660 are positive, resulting in a positive depth correlation. These scenarios are illustrated in quadrants I and III in Fig. S12, where only the hot mantle case is considered, as expected in hot spots. Furthermore, if the MTZ is normal, no correlation is expected. Similarly, if a temperature anomaly only affects one of the discontinuities, zero correlation is also expected. The velocity models that yield the most accurate time-to-depth conversions are those that tend to reduce the correlation value. These models best explain the velocity structure of the upper mantle.

## 3.1 Time corrections

In our case, the time corrections using the IBEM-P18/S19 model result in stronger negative values than the ones observed for the whole investigated area (Fig. S13). Unlike MIT-P08, which is a global P-wave velocity anomaly model, IBEM-P18/S19 is a regional model that provides both P-wave and S-wave velocity anomalies and has a higher resolution in the region of interest. This is reflected by the magnitude and spatial distribution of the time corrections obtained with both models. The time corrections obtained with the IBEM-P18/S19 model have larger absolute values

and are more localized, while the corrections obtained with MIT-P08 due to its lower resolution are smaller and more homogeneously distributed throughout the region.

In particular, for the P410s and P660s phases, the corrections provided by both models seem to disagree more for Madeira (Fig. S14), where IBEM-P18/S19 provides negative corrections with much larger absolute values than those supplied by MIT-P08.

MIT-P08 likely underestimates the time corrections and that the real depth values are shallower than the estimated values**, especially** for Madeira, where the discrepancy with the corrections provided by IBEM-P18/S19 is larger. Due to its higher resolution, we expect the time corrections obtained with IBEM-P18/S19 to be more reliable. However, this model does not cover the whole study region (the western boundary is at a longitude of -19 degrees) and therefore we do not use it to obtain the depths. Still, we can use it to evaluate the robustness of the estimated depth values that we obtain with MIT08.

### 3.2 Correlation analysis

Fig. S15 illustrates the correlation between the topography of the 410 and 660 discontinuities as obtained from the ak135, MIT-P08, and IBEM-P18/S19 models. It should be noted that only the depth values corresponding to the points within the zone covered by the three velocity models were considered. To conduct this statistical analysis, we use interpolated depth values, and we employed the Pearson correlation coefficient as a measure of linear correlation.

For the Canaries, we find that the three models show similar small values for the Pearson correlation coefficient ($\sim 0.2$). This means that changes in the depth values of the 410 are not linearly related to changes in the depth values of the 660. Nevertheless, depth values with the three models show a similar trend: the 410 is deeper, and the 660 is shallower. Considering the smallest correlation value, model IBEM-P18/S19 seems to provide higher quality in depth conversion (Pearson's $r = 0.16$). Furthermore, upon comparing the plots of ak135 and MIT-P08 or ak135 and IBEM-18/19, it is noteworthy that the time corrections provided by MIT-P08 and IBEM-18/19 result in a slight elevation of the 660 discontinuity. This aligns with the expected effect of the negative sign of the time corrections associated with this model. Beneath the Canary Islands, IBEM-P18/S19 exhibits a negative (hot) anomaly extending from the surface to below the transition zone. The negative correlation in the topography of the discontinuities beneath the Canary Islands suggests

that the dominant mineral influencing the topography of both discontinuities in the transition zone is olivine. The sharpness analysis provides additional support to this conclusion, as it reveals clear and well-defined 660 discontinuity features, which is in contrast to a broad 660 that would arise due to garnet being the dominant mineral. Regarding the estimated depths in the results section using MIT-P08, we should take into account that the time corrections are likely underestimated since Pearson's r value is slightly positive (quadrant I in Fig. S12). However, the overall finding remains unchanged, on average the 410 is deeper than the reference value, and the 660 is shallower.

Regarding Madeira, the correlation analysis also reveals no strong linear correlation in discontinuity topography. Our observations show that while the 660 is close to the reference value, the 410 is found at greater depths. The IBEM-P18/S19 model exhibits a negative (hot) anomaly extending from the surface to approximately 300 km depth. If this anomaly also affects the upper part of the transition zone, it would explain the deeper 410 discontinuity, the 660 discontinuity close to the reference value, and the lack of correlation in the topography.

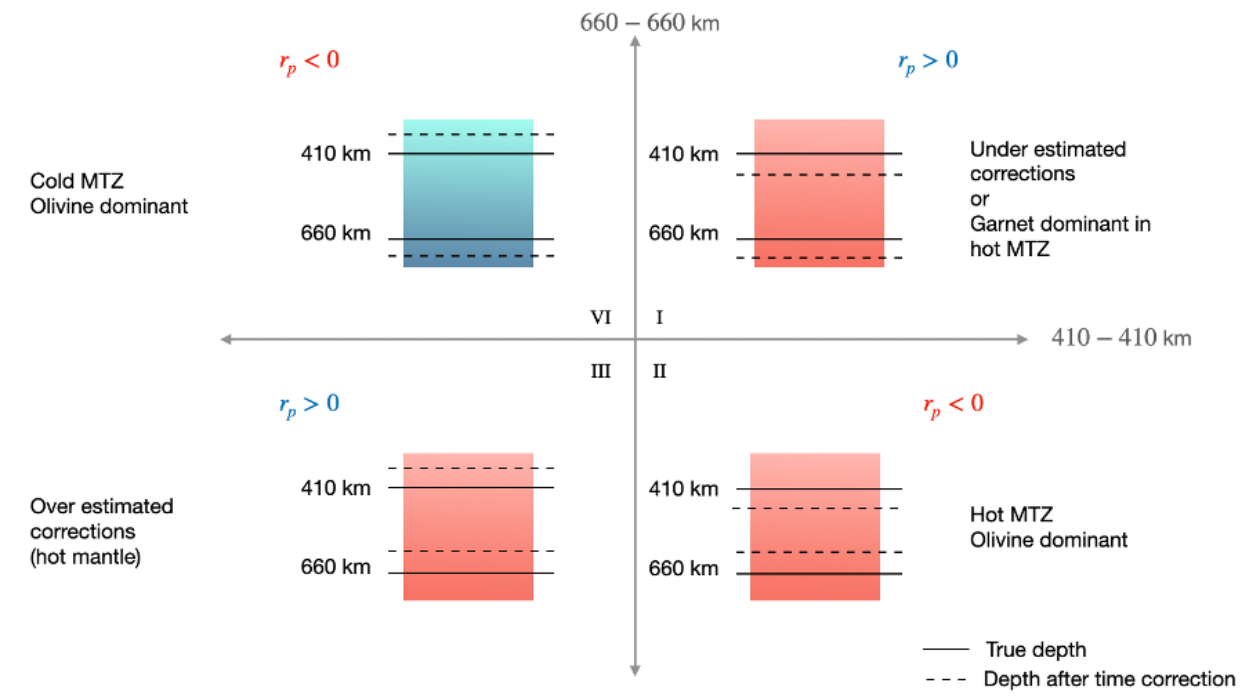


Figure S12: Possible scenarios resulting from the relative topography of the 410 and 660. Variable $r_p$ corresponds to the correlation coefficient.

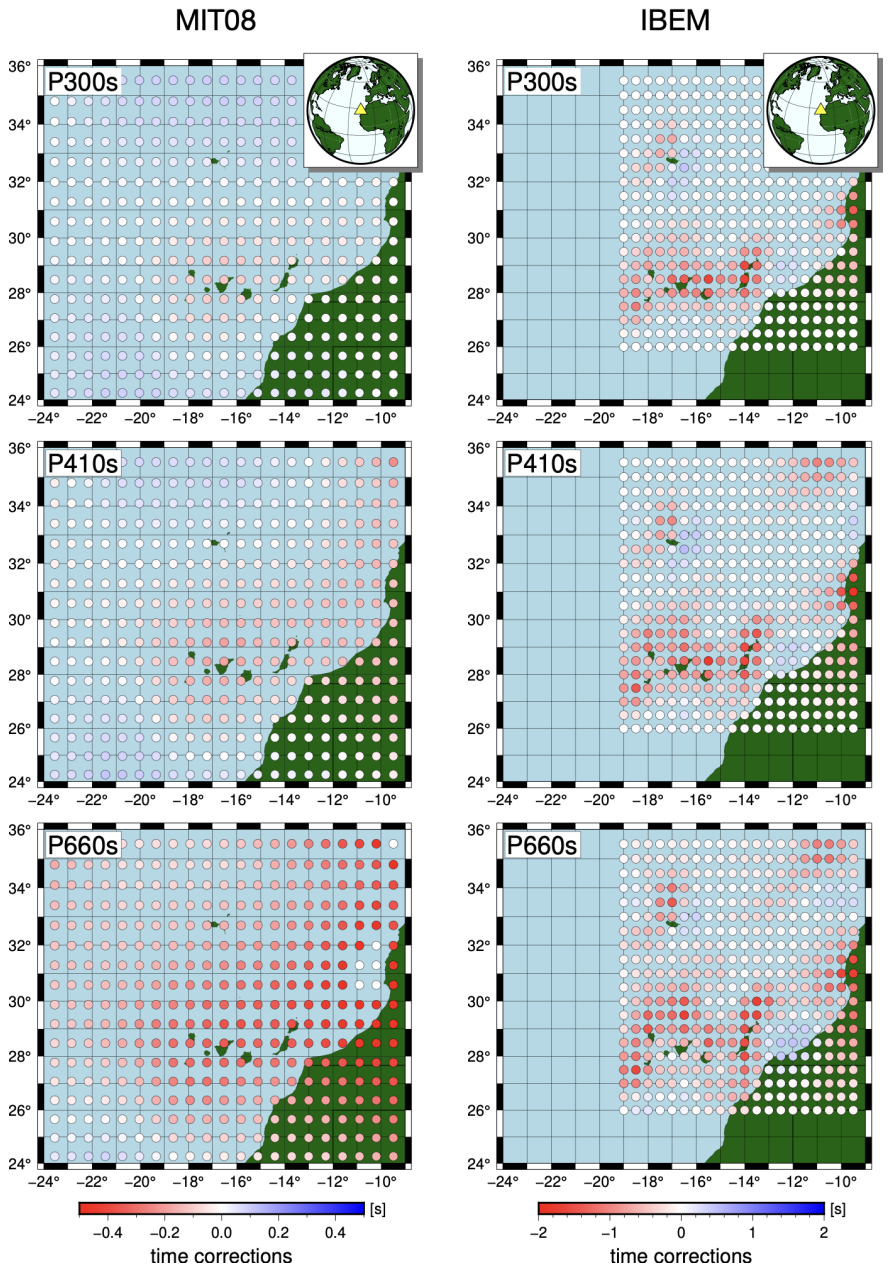


Figure S13: Maps showing the spatial distribution of time corrections obtained with tomography models.MIT08 (on the left) and IBEM-P18/S-19 (on the right).

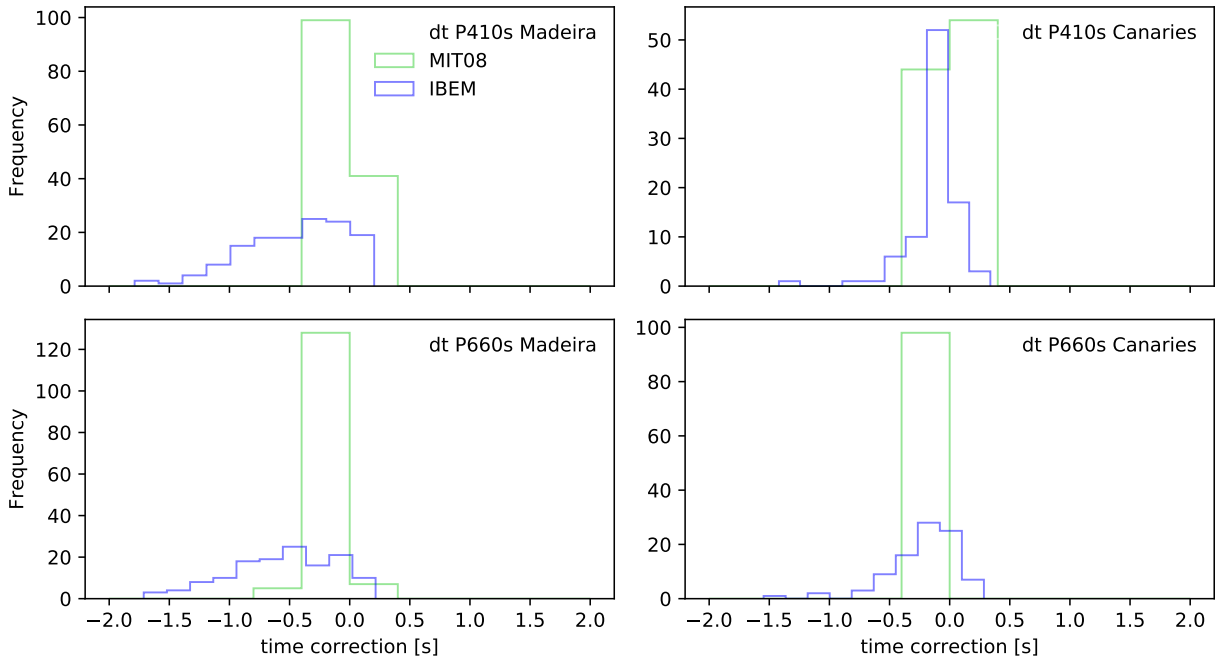


Figure S14: Histograms of time corrections obtained with tomography models.

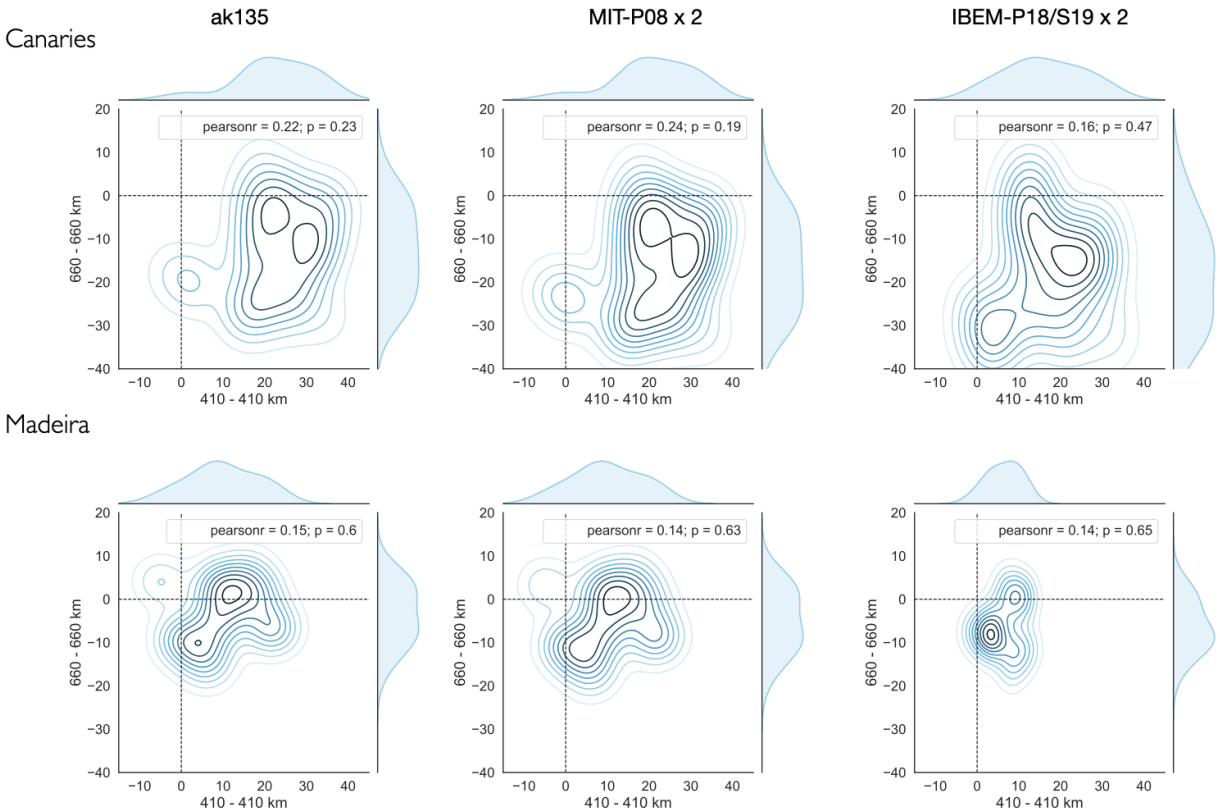


Figure S15: Correlation analysis of 410 and 660 topography.

Table S2: Clapeyron slopes ($\gamma$) of the 410 and 660

| Discontinuity | phase transition[a] | $dP/dT$ (MPa/K) | Reference |
|---|---|---|---|
| 410 | ol→wd | +3.1 | (Akaogi et al., 2007) |
| | | +4.0 | (Katsura et al., 2004; Y. Yu et al., 2008) |
| 660 | rw → brg + fp | -2.6 | (Akaogi et al., 2007) |
| | | -2.0 | (Litasov et al., 2005; Y. G. Yu et al., 2011) |

[a] ol: olivine, wd: wadsleyite, rw: ringwoodite, brg: bridgmanite, and fp: ferropericlase.

Table S3: Possible mechanisms for 300-km discontinuity or X

| **Mechanism** | **Description** | **Reference** |
|---|---|---|
| Formation of hydrous phase A in subduction zones | The formation of hydrous phase A occurs at relatively low mantle temperatures in subduction zones and is not stable at elevated mantle temperatures, such as those expected beneath hotspots (Revenaugh and Jordan, 1991). | Akaogi and Akimoto, 1980; Revenaugh and Jordan, 1991 |
| Orthorhombic to monoclinic phase transition in pyroxene (or pyroxene transition) | The crystallographic transition in pyroxene from an orthorhombic to high-pressure monoclinic phase transition occurs near 300 km depth (Woodland, 1998). However, the impedance contrast ($\sim$ 0.7%; Woodland, 1998) is too low to explain the observed amplitudes of $PXs$ between $\sim$2-8% of the direct P-wave (Kemp et al., 2019; Pugh et al., 2021; Schmerr, 2015). | Woodland, 1998 |
| Transformation of forsterite and periclase to anhydrous phase B | The transformation of forsterite and periclase to anhydrous phase B is possible between 275-345 km, according to mineral physics experiments (Ganguly and Frost, 2006). However, this transformation requires the presence of fluid or hydrous melt and is therefore limited to subcontinental or subduction zone settings (Ganguly and Frost, 2006). Furthermore, it has a weak impedance contrast similar to the pyroxene transition (Chen et al., 2015). | Ganguly and Frost, 2006 |
| Coesite to stishovite phase transition (PT) in eclogite | Stishovite formation requires the presence of eclogite (unequilibrate basalt), suggesting a local enrichment of this mineral in the upper mantle. (Liu et al., 1996). First-principles calculations indicate that the coesite to stishovite PT can take place in a mechanical mixture of basalt and harzburgite that is in disequilibrium. (Xu et al., 2008). It has been demonstrated that by varying the proportion of basalt in the mechanical mixture, the coesite to stishovite phase transition can be seismically observed when the basalt component exceeds 40%. (Kemp et al., 2019). In addition, mineral physics experiments confirm the dependence of P and S-wave velocity contrast with $SiO_2$ content (Chen et al., 2015). | Williams and Revenaugh, 2005 |

# References


Akaogi, M., Takayama, H., Kojitani, H., Kawaji, H., & Atake, T. (2007). Low-temperature heat capacities, entropies and enthalpies of $Mg_2SiO_4$ polymorphs, and $\alpha - \beta - \gamma$ and post-spinel phase relations at high pressure. *Phys Chem Minerals*, *34*, 169–183. https://doi.org/10.1007/s00269-006-0137-3

Akaogi, M., & Akimoto, S.-I. (1980). High-pressure stability of a dense hydrous magnesian silicate $Mg_{23}Si_8O_{42}H_6$ and some geophysical implications. *Journal of Geophysical Research: Solid Earth*, *85*(B12), 6944–6948. https://doi.org/10.1029/JB085iB12p06944

Allen, R. V. (1978). Automatic earthquake recognition and timing from single traces. *Bulletin of the Seismological Society of America*, *68*(5), 1521–1532. https://doi.org/10.1785/BSSA0680051521

Bonatto, L., Schimmel, M., Gallart, J., & Morales, J. (2015). The upper-mantle transition zone beneath the Ibero-Maghrebian region as seen by teleseismic *Pds* phases [Special issue on Iberia geodynamics: An integrative approach from the Topo-Iberia framework]. *Tectonophysics*, *663*, 212–224. https://doi.org/10.1016/j.tecto.2015.02.002

Bonatto, L., Piromallo, C., & Cottaar, S. (2020). The Transition Zone Beneath West Argentina-Central Chile Using P-to-S Converted Waves. *Journal of Geophysical Research: Solid Earth*, *125*(8), e2020JB019446. https://doi.org/10.1029/2020JB019446

Boyce, A., & Cottaar, S. (2021). Insights Into Deep Mantle Thermochemical Contributions to African Magmatism From Converted Seismic Phases. *Geochemistry, Geophysics, Geosystems*, *22*(3), Article e2020GC009478, e2020GC009478. https://doi.org/10.1029/2020GC009478

Chen, T., Gwanmesia, G. D., Wang, X., Zou, Y., Liebermann, R. C., Michaut, C., & Li, B. (2015). Anomalous elastic properties of coesite at high pressure and implications for the upper mantle X-discontinuity. *Earth and Planetary Science Letters*, *412*, 42–51. https://doi.org/10.1016/j.epsl.2014.12.025

Clayton, R. W., & Wiggins, R. A. (1976). Source shape estimation and deconvolution of teleseismic body waves. *J. R. Astr. Soc.*, *47*(1), 151–177. https://doi.org/10.1111/j.1365-246X.1976.tb01267.x

Dueker, K. G., & Sheehan, A. F. (1998). Mantle discontinuity structure beneath the Colorado Rocky Mountains and High Plains., *103*(B4), 7153–7169. https://doi.org/10.1029/97JB03509

Ganguly, J., & Frost, D. J. (2006). Stability of anhydrous phase B: Experimental studies and implications for phase relations in subducting slab and the X discontinuity in the mantle. *Journal of Geophysical Research: Solid Earth*, *111*(B6). https://doi.org/10.1029/2005JB003910

Katsura, T., Yamada, H., Nishikawa, O., Song, M., Kubo, A., Shinmei, T., Yokoshi, S., Aizawa, Y., Yoshino, T., Walter, M. J., & Ito, E. (2004). Olivine-wadsleyite transition in the system $(Mg,Fe)_2SiO_4$. *J. Geophys. Res.*, *109*, B02209. https://doi.org/10.1029/2003JB002438

Kemp, M., Jenkins, J., Maclennan, J., & Cottaar, S. (2019). X-discontinuity and transition zone structure beneath hawaii suggests a heterogeneous plume. *Earth and Planetary Science Letters*, *527*, 115781. https://doi.org/10.1016/j.epsl.2019.115781

Litasov, K. D., Ohtani, E., Sano, A., Suzuki, A., & Funakoshi, K. (2005). Wet subduction versus cold subduction. *Geophysical Research Letters*, *32*(13). https://doi.org/10.1029/2005GL022921

Liu, J., Topor, L., Zhang, J., Navrotsky, A., & Liebermann, R. C. (1996). Calorimetric study of the coesite-stishovite transformation and calculation of the phase boundary. *Phys Chem Minerals*, *23*, 11–16. https://doi.org/10.1007/BF00202988

Pugh, S., Jenkins, J., Boyce, A., & Cottaar, S. (2021). Global receiver function observations of the X-discontinuity reveal recycled basalt beneath hotspots. *Earth and Planetary Science Letters*, *561*, 116813. https://doi.org/10.1016/j.epsl.2021.116813

Revenaugh, J., & Jordan, T. H. (1991). Mantle layering from ScS reverberations: 3. The upper mantle. *Journal of Geophysical Research: Solid Earth*, *96*(B12), 19781–19810. https://doi.org/10.1029/91JB01487

Schmerr, N. (2015). Imaging mantle heterogeneity with upper mantle seismic discontinuities. In A. Khan & F. Deschamps (Eds.), *The earth's heterogeneous mantle: A geophysical, geodynamical, and geochemical perspective* (pp. 79–104). Springer International Publishing. https://doi.org/10.1007/978-3-319-15627-9$_$3

Williams, Q., & Revenaugh, J. (2005). Ancient subduction, mantle eclogite, and the 300 km seismic discontinuity. *Geology*, *33*(1), 1–4. https://doi.org/10.1130/G20968.1

Woodland, A. B. (1998). The orthorhombic to high-P monoclinic phase transition in Mg-Fe Pyroxenes: Can it produce a seismic discontinuity? *Geophysical Research Letters*, *25*(8), 1241–1244. https://doi.org/10.1029/98GL00857

Xu, W., Lithgow-Bertelloni, C., Stixrude, L., & Ritsema, J. (2008). The effect of bulk composition and temperature on mantle seismic structure. *Earth and Planetary Science Letters*, *275*(1), 70–79. https://doi.org/10.1016/j.epsl.2008.08.012

Yu, Y., Wu, Z., & Wentzcovitch, R. (2008). $\alpha - \beta - \gamma$ transformations in Mg2SiO4 in Earth's transition zone. *Earth Planet. Sci. Lett*, *273*, 115–122. https://doi.org/10.1016/j.epsl.2008.06.023

Yu, Y. G., Wentzcovitch, R. M., Vinograd, V. L., & Angel, R. J. (2011). Thermodynamic properties of $MgSiO_3$ majorite and phase transitions near 660 km depth in $MgSiO_3$ and $Mg_2SiO_4$: A first principles study. *Journal of Geophysical Research (Solid Earth)*, *116*(B2), B02208. https://doi.org/10.1029/2010JB007912